

Performance Analysis of Active Shape Reconstruction of Fractured, Incomplete Skulls

Kun Zhang, Wee Kheng Leow, and Yuan Cheng

Dept. of Computer Science, National University of Singapore
zhangkun, leowwk, cyuan@comp.nus.edu.sg

Abstract. Reconstruction of normal skulls from deformed skulls is a very important but difficult task in practice. Active shape model (ASM) is among the most popular methods for reconstructing skulls. To apply ASM to skull reconstruction, it is necessary to establish shape correspondence among the training and testing samples because wrong correspondence will introduce unwanted shape variations in ASM reconstruction. Despite the popularity of ASM, the accuracy of ASM skull reconstruction has not been well investigated in existing literature. In particular, it is unclear how to estimate the reconstruction error of skulls without ground truth. This paper aims to investigate the source of error of ASM skull reconstruction. Comprehensive tests show that the error of accurate correspondence algorithm is uncorrelated and small compared to reconstruction error. On the other hand, ASM fitting error is highly correlated to reconstruction error, which allows us to estimate the reconstruction error of real deformed skulls using ASM fitting error. Moreover, ASM fitting error is correlated to the severity of skull defects, which places a limit on the reconstruction accuracy that can be achieved by ASM.

1 Introduction

Practitioners in surgery, forensics, and anthropology often encounter subjects whose skulls are incomplete and fractured due to impact injury, criminal acts, or natural processes. An important task in these practices is to reconstruct normal, complete skulls from the subjects' deformed (incomplete, fractured) skulls, in the absence of their original complete skull models. The reconstruction process has to predict the skulls' normal shapes from the normal parts of the deformed skulls. Although human skulls have the same global structure, they differ greatly in shape details among people with different races, genders, and ages. Therefore, reconstructing normal skulls from deformed skulls is a very difficult task.

Active shape model (ASM) is among the most popular methods for reconstructing skulls [10, 15, 21]. To build an ASM of the skull from a set of training samples, it is necessary to first establish the shape correspondence among the training samples. Wrong correspondences will introduce unwanted shape variations in ASM. During skull reconstruction, correspondence between the target skull and the ASM needs to be established before ASM can be fitted to the target skull to produce the reconstructed skull. In some applications, such as

face recognition and camera self-calibration, a set of sparse correspondences is sufficient. Skulls, on the other hand, have very complex shape and usually have more than 10000 mesh vertices. Therefore, dense correspondence is required.

Despite the popularity of ASM, the accuracy of skull reconstruction based on ASM has not been well investigated in existing literature such as [10, 15, 21]. It is unknown whether dense correspondence or ASM fitting contributes more error to skull reconstruction. With two sources of error, it is also unknown how to estimate the error of skull reconstruction without ground truth.

This paper aims to investigate the source of error of ASM skull reconstruction and to develop a method for estimating reconstruction error of deformed skulls without ground truth. Our investigation thus contributes to practical application of ASM reconstruction by providing good error estimates.

Note that bones have measurable thickness. Therefore 3D skull models have inner and outer surfaces. In applications such as surgery planning, forensic investigation and anthropology, only the outer surfaces are important because they define the shape appearance of faces. So, this paper focuses on the outer surfaces, which can be easily extracted from the skull models.

2 Related Work

2.1 Reconstruction of Deformed Skulls

Several approaches have been developed for skull reconstruction. A commonly used approach is symmetric-based reconstruction [7, 9, 14], which reflects the normal bones on one side of a skull about the lateral symmetric plane to serve as the reconstruction of the defective parts on the opposite side. When both sides are defective, which is common in practice, this approach cannot be applied.

Geometric reconstruction [2, 11, 20] deforms a reference skull model to register to the normal parts of a deformed skull, and outputs the registered reference model as the reconstructed model. The accuracy of this approach depends highly on the similarity between the reference and deformed skulls as well as the correlation between the normal and defective parts.

Statistical reconstruction [10, 15, 21] overcomes the weaknesses of the other approaches. Instead of using a single reference skull model, this approach constructs a statistical model of possible variations of human skulls. Given a target deformed skull, this approach fits the statistical model to the normal parts of the target skull, and outputs the fitted model as the reconstructed skull. In this paper, we adopt the active shape model in a way similar to [10, 15, 21].

2.2 Dense Correspondence

There are three approaches for computing dense correspondence between two shape models. Among them, non-rigid mesh registration is the predominant approach. Non-rigid registration such as [4, 5, 17, 18, 22] can achieve close matching but needs landmarks to guide the deformation and matching process. Methods

that use manually labeled landmarks [5, 6] are accurate, but manual labeling is too tedious for the entire skull. On the other hand, methods that automatically detect correspondence based on local geometric features [19] are easy to apply but are sensitive to noise and outliers, which can adversely affect their accuracy.

Surface parameterization [3, 8] and group representation [13] are two other approaches for computing dense correspondence. Although they have good theoretical foundation, they are applicable only to simple shapes without holes. It is technically very difficult to apply them to complex shapes such as skulls.

In this paper, we adopt the Thin-Plate Spline (TPS) method developed in our previous work [22] for dense correspondence. Unlike existing TPS methods, our method combines both hard and soft constraints to ensure anatomically consistent correspondence and close matching between the reference and target.

3 Skull Reconstruction Method

Our method consists of three main algorithms: (1) establishing dense correspondence among skull models, (2) building active shape model (ASM) from normal training samples, and (3) fitting ASM to target skull model, which may be fractured and incomplete, to reconstruct a normal model.

3.1 Dense Correspondence

In [22], we propose a method that performs non-rigid registration of a reference model to a target model using Thin-Plate Spline (TPS). The method uses anatomical landmarks as hard constraints to ensure **anatomically consistent correspondence**, and samples control points on skull surfaces to serve as soft constraints, which provide local shape constraints for **close matching** of reference and target surfaces. For normal skulls, it can automatically detect the anatomical landmarks required. For deformed skulls, it requires manually labeled landmarks because the automatic algorithm is not accurate enough for severely deformed skulls. The method adopts a multi-stage coarse-to-fine approach, which consists of the following steps:

1. Apply fractional iterative closest point (FICP) algorithm [16] to register the reference mesh to the target mesh. FICP is more robust than ICP in handling meshes with noise and outliers.
2. Identify anatomical landmarks on the target by manual labeling or automatic detection.
3. Apply TPS to register the reference to the target with anatomical landmarks as hard constraints.
4. Sample control points on reference mesh surfaces and map them to the closest target mesh surfaces.
5. Apply TPS with anatomical landmarks as hard constraints and control points as soft constraints.
6. Resample target mesh by mapping reference mesh vertices and mesh connectivity to the target.

Step 6 ensures that the resampled target has the same number of mesh vertices and mesh connectivity as the reference. For each vertex on the reference mesh, its nearest point on the target mesh within a fixed distance and with a sufficiently similar surface normal is selected as the corresponding point. In the current implementation, the fixed distance is set to 10 mm and the surface normals are similar enough if the cosine of the angle between them is larger than 0.86. For a normal target mesh, if a corresponding point that satisfies these criteria cannot be found, then the nearest target point is used as the corresponding point because there should be no missing correspondence in normal skulls. On the other hand, for a deformed target mesh, if a corresponding point that satisfies these criteria cannot be found, then the corresponding point is regarded as a *missing vertex*. Test results [22] show that our method is more accurate than other TPS methods that use only hard constraints or soft constraints but not both.

3.2 Building Active Shape Model

After establishing dense correspondence between the training samples, they are arranged as column vectors called *shape vectors* in a matrix. Principal Component Analysis is applied to the matrix to compute the *mean shape* $\bar{\mathbf{s}}$ and identify the major components which form the *model matrix* Φ . In our study (Section 4), we used 34 normal skulls as training samples, and 25 components were enough to achieve an unaccounted variance of less than 3%.

3.3 Active Shape Skull Reconstruction

Skull reconstruction is achieved by fitting the skull ASM to a target skull. For a normal target skull, standard ASM fitting is appropriate. For a deformed target skull, the skull ASM is fitted only to the normal parts of the target because the defective parts are either missing or fractured, which distort the skull shape. This approach is similar to those of [10, 15], but is different from that of [21], which fits ASM to the whole skull including the defective parts.

After resampling, the shape vector of the target skull \mathbf{r} is prepared. Let \mathbf{s}' denote the target shape vector whose coordinates of the defective parts, identified as missing mesh vertices, are set to $(0, 0, 0)$. Let $\bar{\mathbf{s}}'$ and Φ' denote the mean shape and model matrix of ASM whose corresponding rows are set to $\mathbf{0}$ to remove unnecessary constraints on the defective parts. Then the reconstruction problem is formulated as one of recovering the shape parameters \mathbf{b} that best fit \mathbf{s}' :

$$\mathbf{s}' = \bar{\mathbf{s}}' + \Phi' \mathbf{b}. \quad (1)$$

Since Φ' may not have an inverse, the shape parameter \mathbf{b} is recovered using the pseudo-inverse of Φ' :

$$\mathbf{b} = (\Phi'^T \Phi')^{-1} \Phi'^T (\mathbf{s}' - \bar{\mathbf{s}}'). \quad (2)$$

Finally, the reconstructed complete skull \mathbf{s} is recovered using the complete mean shape $\bar{\mathbf{s}}$ and model matrix Φ :

$$\mathbf{s} = \bar{\mathbf{s}} + \Phi \mathbf{b}. \quad (3)$$

In practice, the target skull \mathbf{r} may not be spatially aligned to the model represented by the mean shape $\bar{\mathbf{s}}'$. So, it is necessary to recover the similarity transformation T that best aligns \mathbf{r} to \mathbf{s}' , giving

$$T(\mathbf{r}) = \mathbf{s}' = \bar{\mathbf{s}}' + \mathbf{\Phi}'\mathbf{b}. \quad (4)$$

Thus, the reconstruction of \mathbf{r} is formulated as the problem of determining the similarity transformation T and shape parameters \mathbf{b} that minimize the error E :

$$E = \|\bar{\mathbf{s}}' + \mathbf{\Phi}'\mathbf{b} - T(\mathbf{r})\|^2. \quad (5)$$

Equation 5 is minimized using an iterative algorithm adapted from [1]:

ASM Fitting Algorithm

1. Initialize shape parameters \mathbf{b} to zero, and set the reconstructed shape \mathbf{s} as the mean shape $\bar{\mathbf{s}}$ (Eq. 3).
2. Repeat until convergence:
 - (a) Compute the similarity transformation T that best aligns \mathbf{r} to \mathbf{s} by minimizing $\|T(\mathbf{r}) - \mathbf{s}\|^2$.
 - (b) Compute shape parameters $\mathbf{b} = (\mathbf{\Phi}'^T \mathbf{\Phi}')^{-1} \mathbf{\Phi}'^T (T(\mathbf{r}) - \bar{\mathbf{s}}')$ (Eq. 2).
 - (c) Compute the reconstructed shape $\mathbf{s} = \bar{\mathbf{s}} + \mathbf{\Phi}\mathbf{b}$ (Eq. 3).

4 Experiments and Discussions

4.1 Data Preparation and Test Procedure

A comprehensive set of experiments was conducted to evaluate the skull reconstruction algorithm. ASM of skull was constructed using 34 normal, complete skulls. 8 other normal, complete skulls were used as testing samples (Fig. 1(1; a–b)). They were flipped about their lateral symmetric planes to create additional test samples. As human skulls are not exactly left-right symmetric, the number of complete, normal test samples were doubled in this way to 16.

The 16 complete, normal testing samples were used to generate synthetic fractured, incomplete testing samples. To study how the severity of defects affects reconstruction result, synthetic skulls with four levels of severity were created: mild, moderate, severe, and very severe. The first three levels were either fractured or incomplete. For each of the first three levels, the skulls were manually fractured at three places: cranial, facial, and jaw bones (Fig. 1(2–4; a–c)), in a manner similar to real fractures. Incomplete skull samples were created by removing the fractured bone fragments (Fig. 1(2–4; d–f)). These incomplete cases may occur in forensic investigation due to criminal acts and surgery due to removal of defective parts. Additional incomplete skulls were created by removing the top of the cranial bone or the bottom of the lower jaw (Fig. 1(1, 5; d–f)). These situations could happen in real applications due to CT scanning limits while scanning the patients. The very severe testing samples had multiple defects of fractures and missing parts (Fig. 1(5; a–b)). In total, each of the first

three levels of severity had 128 ($=16 \times (3+5)$) synthetic samples, and the fourth level of severity had 32 ($=16 \times 2$) synthetic samples. In addition, 6 other fractured, incomplete skulls constructed from patients' CT volumes were used as real testing samples (Fig. 2). They had different degrees of fracture and incompleteness. In summary, there were 34 normal, complete training samples; 16 normal, complete testing samples; 416 ($=128 \times 3 + 32$) synthetic fractured, incomplete testing samples; and 6 real fractured, incomplete testing samples.

For the experimental procedure, first, dense correspondence was applied to resample the training samples (Section 3.1). Next, the skull ASM was constructed using the resampled training samples (Section 3.2). Next, dense correspondence algorithm was applied to resample the testing samples and identify their normal parts (Section 3.1). Finally, normal skulls of the testing samples were reconstructed by fitting the skull ASM to the resampled testing samples (Section 3.3).

Three kinds of errors were measured: resampling error, ASM fitting error, and reconstruction error. Resampling error E_S measured the difference between the target skull model and its resampled mesh using mean surface distance:

$$E_S = \frac{1}{m} \sum_{j=1}^m \|\mathbf{u}_j - \mathbf{p}_j\|, \quad (6)$$

where \mathbf{u}_j was a mesh vertex on the target skull and \mathbf{p}_j was its nearest surface point on the resampled mesh. It measured the combined error of correspondence building and mesh resampling. Resampling errors of the defective and normal parts of a target skull were measured separately because the defective parts were expected to have larger resampling error compared to the normal parts.

ASM fitting error measured the difference between the resampled mesh and the mesh reconstructed by ASM fitting. Two measurement methods were adopted. The first method measured the mean displacement of mesh vertices:

$$E_F = \frac{1}{n} \sum_{i=1}^n \|\mathbf{v}_i - \mathbf{v}'_i\|, \quad (7)$$

where \mathbf{v}_i was a mesh vertex on the resampled mesh and \mathbf{v}'_i was its corresponding vertex on the reconstructed mesh. This formulation of ASM fitting error measured the average mesh vertex displacement as a result of ASM fitting. So, it evaluated the amount of shape change incurred in the ASM fitting process.

The second method measured the mean surface distance:

$$E_G = \frac{1}{n} \sum_{i=1}^n \|\mathbf{v}_i - \mathbf{p}'_i\|, \quad (8)$$

where \mathbf{v}_i was a mesh vertex on the resampled mesh and \mathbf{p}'_i was its nearest surface point on the reconstructed mesh. This formulation was appropriate since it was consistent and thus comparable to the resampling error and reconstruction error.

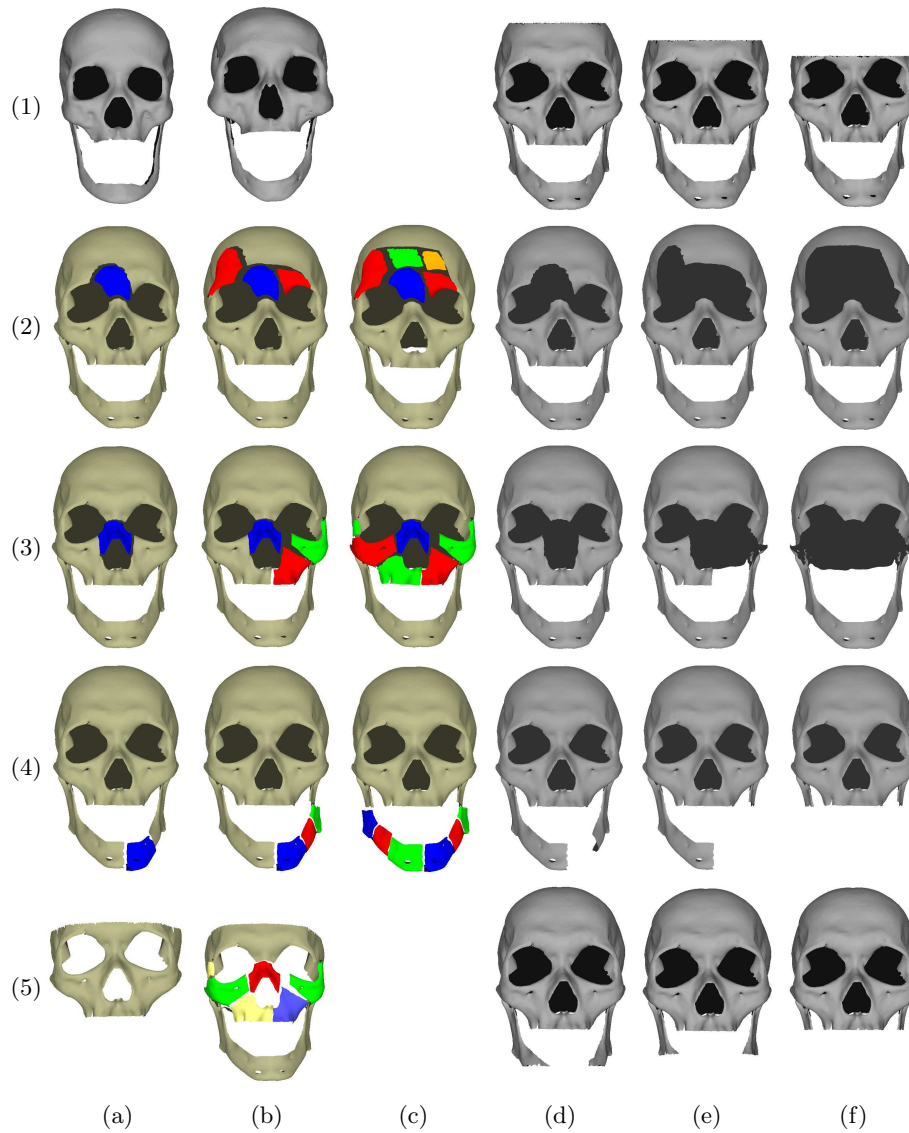


Fig. 1. Examples of synthetic testing samples. (1; a–b) Normal, complete skulls. (2–4; a–c) Skulls with mild, moderate, and severe fractures at different locations. (1–5; d–f) Skulls with mild, moderate, and severe missing parts at different locations. (1, 5; d–f) Incompleteness due to scan limits. (2–4; d–f) Incompleteness due to fractures. (5; a–b) Very severe cases with multiple defects.

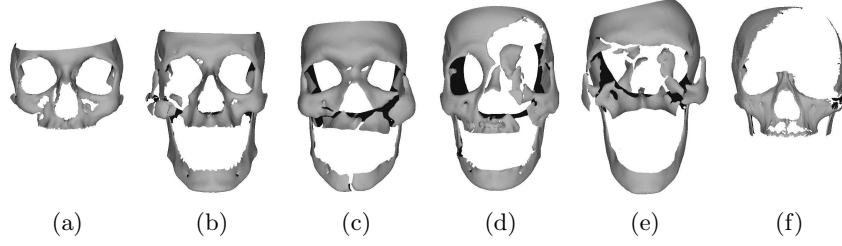


Fig. 2. Examples of real testing samples constructed from patients’ CT images. They have different severities of fractures and incompleteness.

Reconstruction error was computed as the mean surface distance between the ground truth and the reconstructed mesh:

$$E_R = \frac{1}{n} \sum_{i=1}^n \|\mathbf{v}_i^* - \mathbf{q}'_i\|, \quad (9)$$

where \mathbf{v}_i^* was a mesh vertex in the ground truth and \mathbf{q}'_i was its nearest surface point on the reconstructed mesh.

4.2 Test Results

Figure 3 shows that the resampling error of the training samples and the testing samples is very small, mostly ranging from 0.1 mm to 0.34 mm. Moreover, it is not correlated to the severity of skull defects and reconstruction error E_R . When measured separately, test results show that the resampling error of the fractured parts is generally larger than that of the normal parts of the same skull, and it ranges from 0.2 mm to 2.3 mm (not shown in Fig. 3). Nevertheless, it is still uncorrelated to the severity of defects.

On the other hand, ASM fitting errors are correlated to the severity of defects (Fig. 4). In particular, training samples have the smallest ASM fitting errors ($E_F < 1.2$ mm, $E_G < 0.5$ mm) as expected. Synthetic testing samples with mild, moderate, and severe defects have E_F ranging from 2.2 mm to 5.3 mm and E_G between 0.9 mm and 1.7 mm, whereas those with very severe defects have E_F of 4.5 mm to 8.0 mm and E_G of 1.4 mm to 2.8 mm. For all samples, E_F , which measures average shape change, is higher than E_G , which measures mean surface distance. This shows that mean surface distance, while easy to measure and commonly used, under-estimates actual shape difference.

ASM fitting error is also strongly correlated to reconstruction error E_R (Fig. 4). Except for some outliers, there is a strong linear relationship between ASM fitting errors (E_F , E_G) and reconstruction error E_R . On the other hand, resampling error E_S is not correlated to reconstruction error E_R and is very small (about 10%) compared to E_R . So, its contribution to E_R can be omitted.

In practice, the reconstruction errors of real deformed samples are unknown because of the absence of ground truth. To the best of our knowledge, nobody

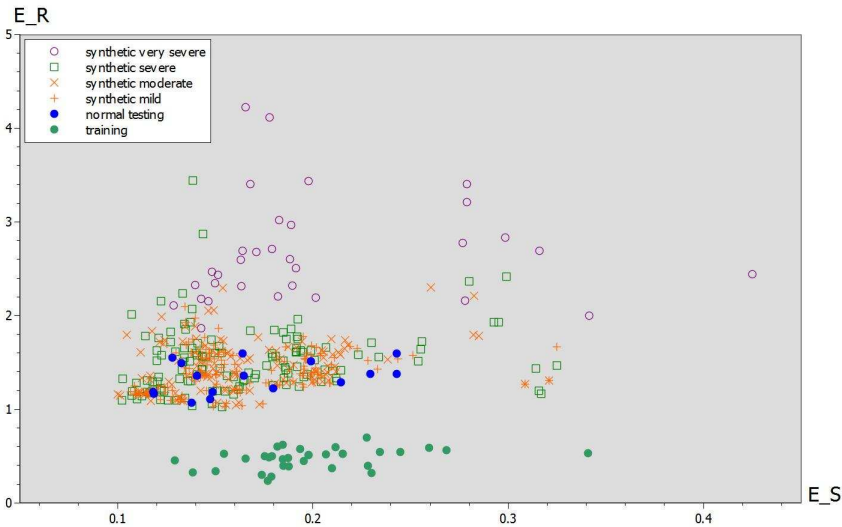


Fig. 3. A plot of resampling error E_S vs. reconstruction error E_R measured in mm.

has attempted to estimate the reconstruction error of real skulls. The linear relationship observed between ASM fitting error and reconstruction error makes it possible to estimate reconstruction error based on ASM fitting error. Using a robust regression method [12], the ASM fitting errors and the reconstruction error of all samples can be fitted to a line. This robust regression method iteratively re-weights each sample and minimizes the weighted sum of squared distance. The weight of each sample ranges from 0 to 1 depending on its distance to the fitted line. With a smaller weight, the sample is more likely to be an outlier.

With two ASM fitting errors E_F and E_G , three lines can be fitted: E_F vs. E_R , E_G vs. E_R , and E_F and E_G vs. E_R . The first two are single-fits whereas the third line is a dual-fit. Since we have no real testing samples with ground truth to determine which of these three methods is the best, all of them are presented in this paper. These fitted lines are evaluated on two criteria: fitting error and possibility of outlier. Fitting error computes the averaged weighted sum of absolute distances of all samples. The possibility of outlier is computed as 1 minus the averaged weight of the samples. Note that this possibility measurement is not strictly a probability. Compared to single-fit with E_F , single-fit with E_G and dual-fit have smaller fitting error but larger possibility of outlier (Table 1). This implies that E_F contributes less than E_G to dual-fit. Further study should be performed to investigate which one of these three fitting methods is better in estimating reconstruction error in real applications.

Using the fitted lines, the estimated reconstruction errors of real testing samples are computed and plotted in Fig. 4. The estimated reconstruction errors vary with severity of skull defects. For example, Fig. 2(a) and 2(f) are the most severely incomplete and have the largest reconstruction errors. The estimated

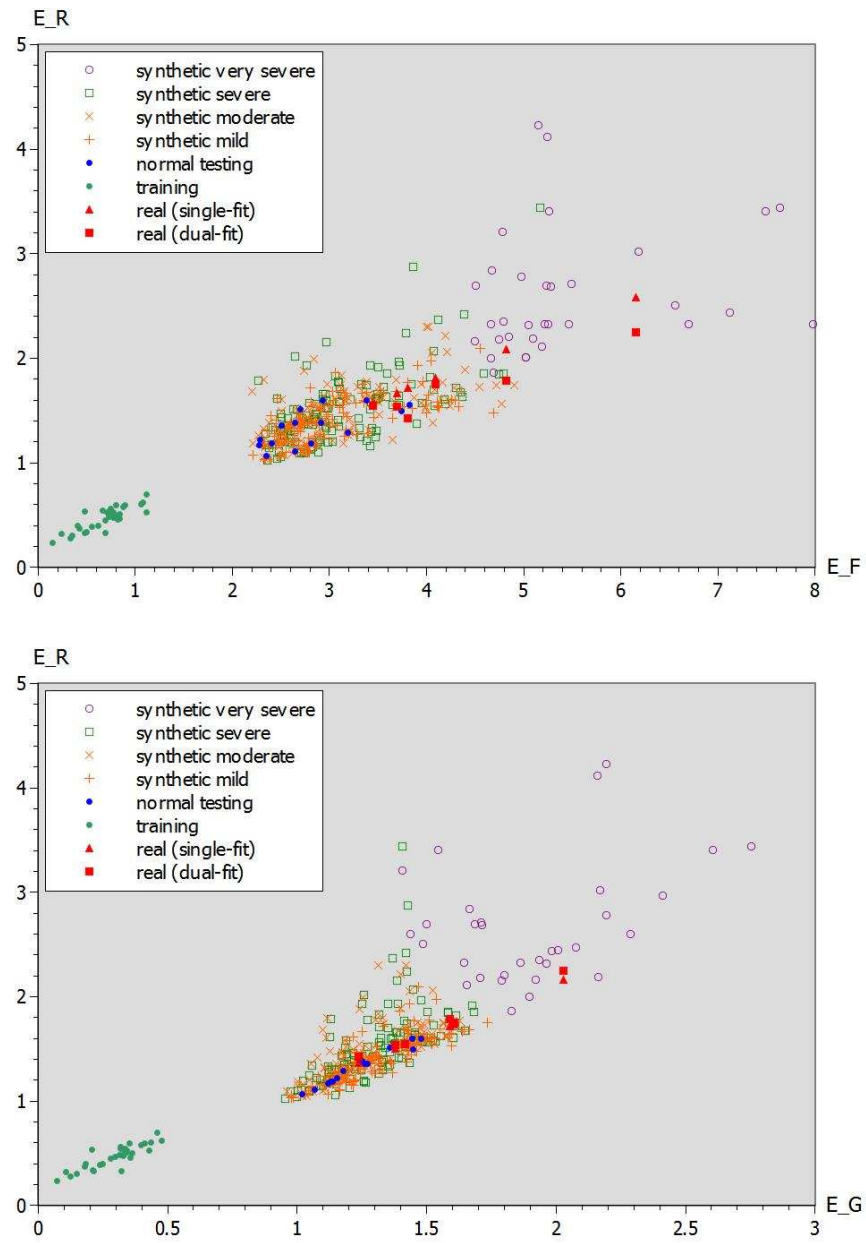


Fig. 4. Plots of ASM fitting error E_F and E_G vs. reconstruction error E_R measured in mm.

Table 1. Evaluation of fitted lines.

Methods	Fitting error (mm)	Possibility of outliers
Single-Fit with E_F	0.14	0.11
Single-Fit with E_G	0.08	0.16
Dual-Fit	0.07	0.16

reconstruction errors of real testing samples are within the range of those of synthetic testing samples, indicating that the estimated errors are reliable.

5 Conclusion

This paper presented a performance analysis of reconstruction of fractured, incomplete skulls using active shape model (ASM). Thin-plate spline (TPS) registration was used to establish dense correspondence and resample skull samples so that they have the same number of mesh vertices and mesh connectivity. The skull ASM was built on resampled training samples and fitted to resampled testing samples to generate reconstructed meshes of testing samples. A comprehensive set of tests was performed on both synthetic and real testing samples. Test results show that resampling error, which measures the combined error of dense correspondence and mesh resampling, is uncorrelated and small (about 10%) compared to reconstruction error. On the other hand, there is a strong linear relationship between ASM fitting error and reconstruction error. These observations allow us to estimate the reconstruction error of real deformed skulls using ASM fitting error alone, which is valuable in practical applications.

Test results also show that ASM fitting error is correlated to the severity of skull defects. This implies that ASM fitting likely fills in average shapes for the defective parts of target skulls while attempting to match the normal parts as closely as possible. This is especially so when the shapes of the normal parts are not strongly correlated to those of the targets to be filled in. For example, it is practically impossible to predict the shapes of the facial bones using only the cranial bones because they are not strongly correlated. As more parts are filled with average shapes, the reconstructed skulls will differ more from ground truth. This observation indicates a limit on the reconstruction accuracy that can be achieved using ASM. To achieve higher reconstruction accuracy, more information about the target skull is needed in the reconstruction process.

References

1. E.R. Baldock and J. Graham. *Image Processing and Analysis: A Practical Approach*. Oxford University Press, 2000.
2. S. Benazzi, E. Stansfield, C. Milani, and G. Gruppioni. Geometric morphometric methods for three-dimensional virtual reconstruction of a fragmented cranium: The case of Angelo Poliziano. *Int. Journal on Legal Medicine*, 123(4):333–344, 2009.

3. C. Bennis. Piecewise surface flattening for non-distorted texture mapping. *Computer Graphics*, 25(4):237–246, 1991.
4. M. Berar, M. Desvignes, G. Bailly, and Y. Payan. 3D meshes registration: Application to statistical skull model. In *Proc. of Image Analysis and Recog.*, 2004.
5. H. Chui and A. Rangarajan. A new algorithm for non-rigid point matching. In *Proc. IEEE Conf. Computer Vision and Pattern Recognition*, 2000.
6. Q. Deng, M. Zhou, W. Shui, Z. Wu, Y. Ji, and R. Bai. A novel skull registration based on global and local deformations for craniofacial reconstruction. *Forensic Science Int.*, 208:95–102, 2011.
7. D.M. Elena, J. Chapuis, I. Pappas, G. Ferrigno, W. Hallermann, A. Schramm, and M. Caversaccio. Automatic extraction of the mid-facial plane for cranio-maxillofacial surgery planning. *Int. J. Oral and Maxillofacial Surgery*, 35(7):636–642, 2006.
8. M.S. Floater and K. Hormann. Surface parameterization: A tutorial and survey. *Advances in Multiresolution for Geometric Modelling*, pages 157–186, 2005.
9. H. K. Gumprecht, D. C. Widenka, and C. B. Lumenta. BrainLab VectorVision Neuronavigation System: Technology and clinical experiences in 131 cases. *Neurosurgery*, 44(1), 1999.
10. P. Gunz. *Statistical and Geometric Reconstruction of Hominid Crania: Reconstructing Australopithecine Ontogeny*. Universität Wien, 2005.
11. P. Gunz, P. Mitteroecker, F. Bookstein, and G. Weber. Computer aided reconstruction of human crania. In *Proc. Computer Applications and Quantitative Methods in Archaeology*, 2004.
12. P.W. Holland and R.E. Welsch. Robust regression using iteratively reweighted least-squares. *Comm. in Statistics: Theory and Methods*, 6(9):813–827, 1977.
13. A.C.W. Kotcheff and C.J. Taylor. Automatic construction of eigenshapemodels by direct optimization. *Medical Image Analysis*, 2(4):303–314, 1998.
14. M.Y. Lee, C.C. Chang, C.C. Lin, L.J. Lo, and Y.R. Chen. Medical rapid prototyping in custom implant design for craniofacial reconstruction. *IEEE Trans. Systems, Man and Cybernetics*, 3:2903–2908, 2003.
15. M. Lüthi, T. Albrecht, and T. Vetter. Building shape models from lousy data. In *Proc. MICCAI*, 2009.
16. J.M. Phillips, R. Liu, and C. Tomasi. Outlier robust ICP for minimizing fractional RMSD. In *Proc. Int. Conf. 3-D Digital Imaging and Modeling*, 2007.
17. H. Seo and N.M. Thalmann. An automatic modeling of human bodies from sizing parameters. In *Proc. ACM SIGGRAPH*, 2003.
18. A. Souza and J.K. Udupa. Automatic landmark selection for active shape models. In *Proc. SPIE Medical Imaging*, 2005.
19. W. D. Turner, R. E. Brown, T. P. Kelliher, P. H. Tu, M. A. Taister, and K. W. Miller. A novel method of automated skull registration for forensic facial approximation. *Forensic Science Int.*, 154:149–158, 2005.
20. L. Wei, W. Yu, M. Li, and X. Li. Skull assembly and completion using template-based surface matching. In *Proc. of Int. Conf. 3D Imaging, Modeling, Processing, Visualization and Transmission*, 2011.
21. S. Zachow, H. Lamecker, B. Elsholtz, and M. Stiller. Reconstruction of mandibular dysplasia using a statistical 3D shape model. In *Computer Assisted Radiology and Surgery*, pages 1238–1243, 2005.
22. K. Zhang, Y. Cheng, and W.K. Leow. Dense correspondence of skull models by automatic detection of anatomical landmarks. In *Proc. Int. Conf. Computer Analysis of Images and Patterns*, 2013.